High Power Laser Science and Engineering, (2018), Vol. 6, e22, 6 pages.

doi:10.1017/hpl.2018.17

Using the ROSS optical streak camera as a tool to understand laboratory experiments of laser-driven magnetized shock waves

Andy Liao[1], Patrick Hartigan[1], Gennady Fiksel[2], Brent Blue[3], Peter Graham[4], John Foster[4], and Carolyn Kuranz[2]

[1]*Rice University, USA*

[2]*University of Michigan - Ann Arbor, USA*

[3]*Lawrence Livermore National Laboratory, USA*

[4]*Awe Plc, UK*

(Received 1 December 2017; revised 22 January 2018; accepted 7 March 2018)

Abstract

Supersonic flows with high Mach number are ubiquitous in astrophysics. High-powered lasers also have the ability to drive high Mach number, radiating shock waves in laboratory plasmas, and recent experiments along these lines have made it possible to recreate analogs of high Mach-number astrophysical flows under controlled conditions. Streak cameras such as the Rochester optical streak system (ROSS) are particularly helpful in diagnosing such experiments, because they acquire spatially resolved measurements of the radiating gas continuously over a large time interval, making it easy to observe how any shock waves and ablation fronts present in the system evolve with time. This paper summarizes new ROSS observations of a laboratory analog of the collision of a stellar wind with an ablating planetary atmosphere embedded within a magnetosphere. We find good agreement between the observed ROSS data and numerical models obtained with the FLASH code, but only when the effects of optical depth are properly taken into account.

Keywords: laser optical systems; plasma astrophysics

1. Introduction

Supersonic, high Mach-number flows are widely implicated in observed astrophysical phenomena. These include supernovae ejecta, accretion inflows, jets and outflows from accretion disks, and some stellar winds[1–8]. When supersonic flows inevitably encounter resistance, they form radiating shock waves that can leave tell-tale signs in emission features across the electromagnetic spectrum[9–12].

On one hand, particulars of these emission features can reveal characteristic flow parameters including density, composition, velocity, temperature, or magnetic flux density and orientation, and any number of derivatives; hence, they can make observations of shock waves understandable in terms of the underlying astrophysics of the flows[13–15]. On the other hand, the connection between observation and astrophysics leans on a theoretical framework that can be obscured by the inherent complexity of real objects and the limited perspective of real observations. Hence, laboratory astrophysics experiments that can recreate and observe these supersonic flows in a controlled setting and in real time can be useful to improve our understanding of the astrophysics underlying real observations.

In our experiments we introduce in Section 2, we use the OMEGA laser to drive highly variable, high Mach-number flows that develop into radiating bow shocks when they encounter an ablating, magnetized, quasi-linear obstacle in the form of a MIFEDS wire[16]. We use the Streaked optical pyrometer (SOP) instrument on the Rochester optical streak system (ROSS) to obtain spatially resolved streak images of the optical sources in the plasma as they develop in real time, and we present these results in Section 3. We show in Section 4 that, with support from predictive numerical simulations computed using the FLASH code[17], our observations on the SOP can be explained only when the instrument's perspective, i.e., the optical depth of gas in its line of sight (LOS), is properly taken into account.

Correspondence to: A. Liao, Rice University HBH 363, 6100 Main Street, Houston, TX 77005, USA. Email: Andy.Liao@rice.edu

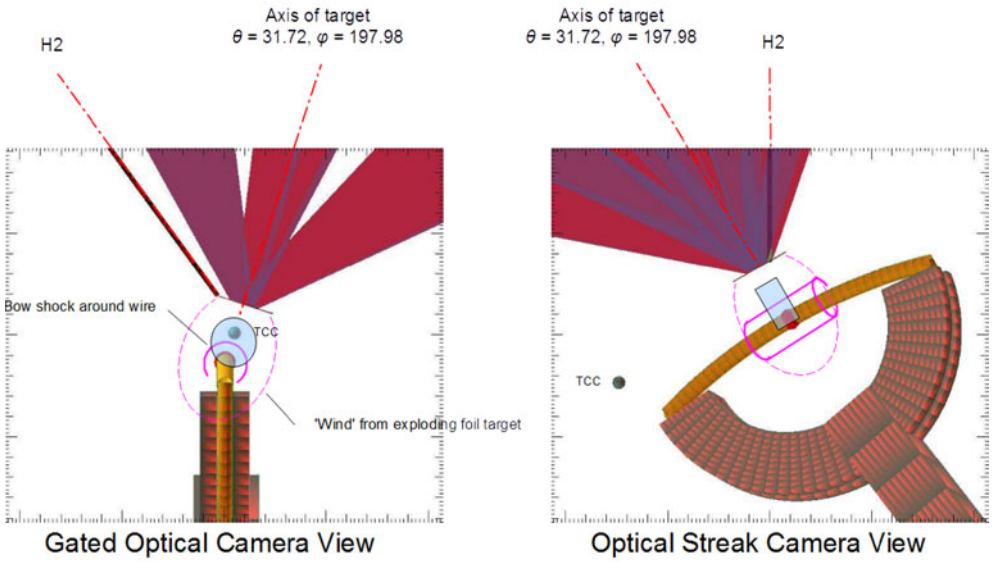

Figure 1. VisRAD drawing shows the experimental assembly from the perspective of optical instruments, and the field of view of these instruments with approximate aim is overlaid. The instruments are set to capture from orthogonal angles the evolution of the high Mach-number laser plume when and where it meets the MIFEDS wire. We mark the target chamber center (TCC) and the pointing (H2) of the target positioning system in either view as spatial cues.

2. Experiment

2.1. Facilities

2.1.1. OMEGA laser

We use the OMEGA laser primarily as an energy-delivery system to drive high Mach-number flows. The OMEGA laser can deliver up to 30 kJ of 351 nm UV laser energy on mm-sized targets across 60 independently targeted and focused beams over pulses lasting 0.5–3 ns. The laser system also allows for staggering in time of laser pulses delivered through each beam, and the laser spot shape on target can also be controlled independently through the use of distributed phase plates (DPPs)[18]. Together, the independent spatial and temporal targeting capability of the OMEGA laser allows for complex experiments to be run. To illustrate: in a single shot, OMEGA can drive high Mach-number flows with one set of beams, and it can diagnose those plasmas by using other sets of beams to power a number of backlit instruments[19, 20].

2.1.2. Streaked optical pyrometer

We use the SOP, the main instrument of the ROSS to continuously assess the time evolution of the spatially resolved source region of self-emission in the experimental plasma[21, 22]. After f/3.3 imaging optics brings the self-emissions to the SOP through an adjustable slit of width 0.5–5 mm, the resulting image is sent to a Photonis P510, P820, or PJX streak tube that forms the core of SOP streak camera. At the streak tube, the image is first converted to a stream of electrons at a S-1 or S-20 photocathode at its front end. Pulse generators drive a ramping electric field inside the streak tube to focus and sweep the electron stream across a phosphor screen. The electrons are converted back into photons at the screen, and regenerated photons finally reach a 4 megapixel CCD, where the streak image is recorded. The SOP can be set to sweep any interval longer than 1 ns. Using a 10 ns sweep interval, the time resolution of the resulting streak image is ∼170 ps with the 0.5 mm slit, and the spatial resolution is $\lesssim$20 μm with the nominal optics.

2.2. Design

The design of our experiment has been illustrated in Figure 1 in the perspectives of both optical instruments including a gated, optical plane imager (TPDI), and the SOP. Together, the lines of sight from each instrument are orthogonal, and the structure of the assembly is unambiguous. Drawings from either perspective show the arrangement of a quasi-linear MIFEDS wire at 3-mm-minimum separation from a planar CH-polymer target of 1.2 g/c density. The target, or foil has dimensions of 3-mm diameter and 50-μm thickness. The MIFEDS wire is an arc of 11 mm over a circle of 25-mm diameter. The wire has a gross thickness of 635 μm, a copper core thickness of 400 μm, and the difference is met by kapton insulation.

In each of ten runs of the experiment, or shots, ten laser beams strike the target, and they deliver a total energy of 4.5 kJ over 1 ns to a centered, 704-μm-diameter, ∼4th-order super-Gaussian spot. The plasma plume that develops from the rear irradiation of the target is directed toward the MIFEDS wire orthogonally from the LOS of either perspective, and we also include the aimpoint and field of

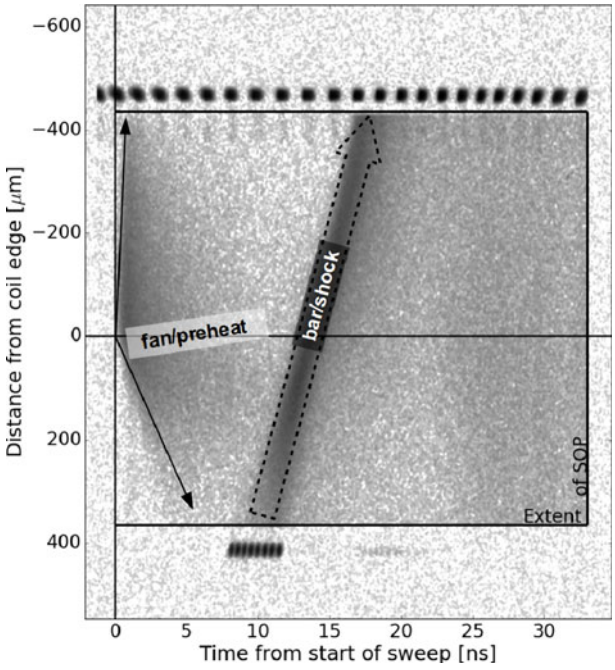

Figure 2. Streak camera image of shot 75081 shows the progress of optical sources near the edge of the MIFEDS arc viewed face-on over a sweep time of 33 ns from initiation of the laser beams driving the plasma.

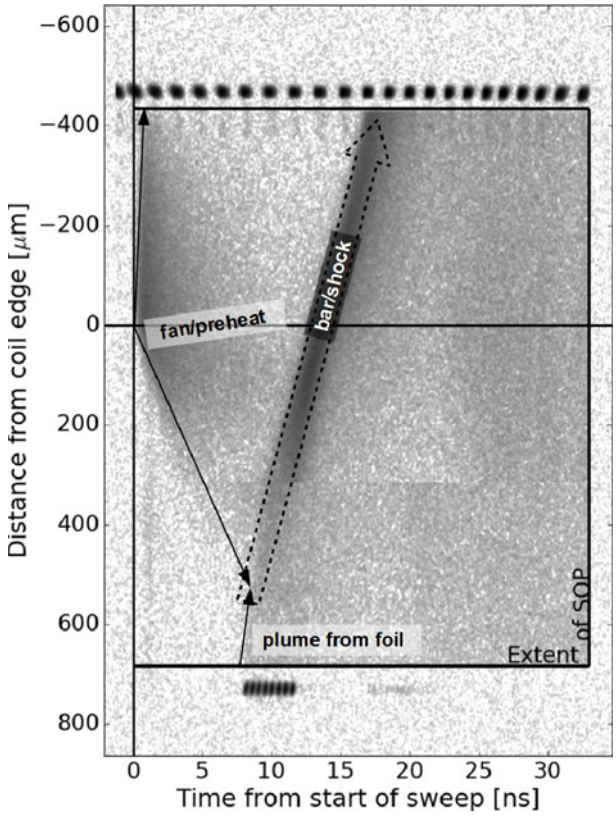

Figure 3. Spatially extended view from the SOP combining streak images from shots 75080 and 75081 shows the interaction dynamics of observed emission features and their originating plasma flows.

view (FOV) of the instruments themselves in transparent blue overlay. The planar 2D imager looks down the arc of the wire aiming just over its edge with a 1.5-mm-diameter aperture. The SOP is a slit of 0.8-mm long and 0.5-mm wide aimed toward the arc of the MIFEDS wire face-on, and it is oriented to resolve the source as it moves down the axis of the laser plume.

In five of ten shots, we charge the MIFEDS capacitor to 18 kV, and a peak current of 30 kA is delivered down the wire on discharge. The discharge current produces a magnetic field pulse that peaks to 19 T at the wire's surface with a flat top, and the peak field is timed to be coincident with the initiation of the laser beams. The duration of the flat top of the magnetic field pulse is ±150 ns relative to the laser initiation, thereby it far exceeds the timescale of the plasma hydrodynamics. In these shots, the laser plume co-evolves with the magnetosphere of the MIFEDS wire, and gasdynamical effects of magnetization can become apparent when the plasma is viewed with the appropriate diagnostics.

3. Results

An SOP streak image consistent with results from eight of ten shots taken is reproduced in Figure 2. In this image, the spatially resolved vertical dimension is aligned with the laser plume axis, and it is zeroed on the target-facing edge of the MIFEDS arc. The full length of the slit – 800 μm – is represented at all times during the sweep. The temporal dimension is horizontal, and time advances from laser initiation at t_0 from left to right over 33 ns.

Sweeping across the streak image, we first see a fan-like source of emissions that originates at t_0 and radiates outward from the edge of the MIFEDS arc. We associate the source of these early emissions with plasma that has been ablated from the wire itself by a radiation precursor ahead of the laser plume. By $t_0 + 10$ ns, we see a second source, a shock emerges from the bottom of the frame, and over the next ∼10 ns, this bar-like feature passes into the foreground of the MIFEDS arc, and its progress is relentless before it moves out of the FOV.

Two of ten shots feature a shift in the aimpoint of the SOP slit away from the MIFEDS arc, and nearer toward the target foil. This adjustment allowed the SOP to capture the behavior of optical sources at earlier times. Combining the views taken from either aimpoint, we obtain the spatially extended view of Figure 3 that reveals the origin of the bar-like shock at the intersection, or collision of two expanding flows near $t_0 + 8$ ns. We derive the slit-projected velocity of each feature from its slope. The outward edge of the preheat fan clocks its expansion at ∼60 km/s, likewise the foil plume clocks in at ∼200 km/s, and the bar-like shock travels at ∼100 km/s.

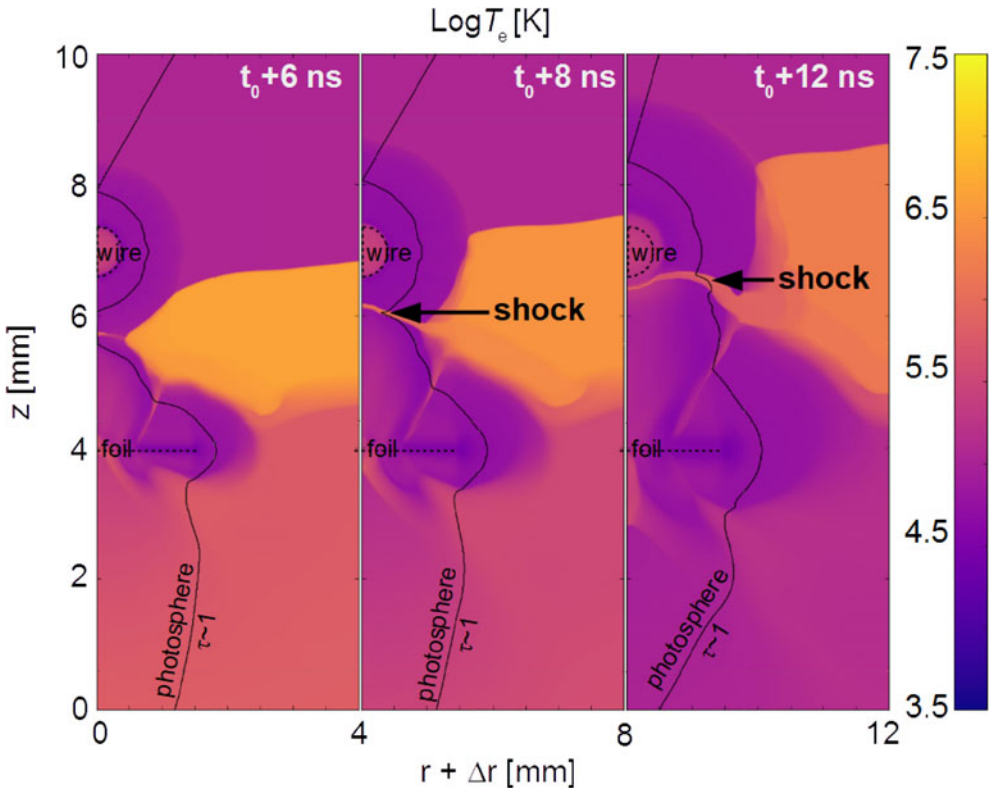

Figure 4. FLASH simulation results in the log T_e distribution through critical epochs show the evolution of emission sources localized to the hottest gas. The planar target is placed on-axis at the $z = 4$ mm position, and the MIFEDS wire profile is centered at $z = 7$ mm. We draw in a black curve to mark the depth of formation of the visible continuum as seen by an instrument viewing the plasma cylinder from the side. This curve also broadly traces the contact discontinuity between the plasma and pseudovacuum.

Per design from Section 2.2 we pulsed the MIFEDS in five of ten shots, and the difference was met by unpulsed shots as controls. Images of the plasma in the pulsed shots are indistinguishable from those of control shots, hence, we infer that the magnetization of the plasma by the MIFEDS was too weak to visibly affect its apparent hydrodynamics.

4. Discussion

At a glance, it was difficult to reconcile the optical sources seen from the SOP and the expected features that connote the development of a radiating bow shock around the MIFEDS wire. In the case of a bow shock, we could expect to see the strongest emissions from the stagnated flow to hover just above the edge of the MIFEDS arc. Instead, the trajectory of the strongest source we identified as a shock in the streak images appears entirely unconcerned with the presence of what should be an impassable obstacle in the plane of the MIFEDS arc. Passage of emission sources into the foreground of the MIFEDS arc is not unexpected, but the apparent absence of any stagnating gas behind the shock was not anticipated in the design.

To satisfactorily reconstruct the experimental hydrodynamics, thereby resolving unforeseen results from our observations of the experimental bow shock, we use the FLASH Eulerian hydrodynamics code to build a realistic numerical model of the experimental radiation hydrodynamics. Our FLASH simulation affords us a view of the experimental plasma that is unconstrained by instrumental limitations in perspective. We apply post-processing, including artificial perspective to the hydrodynamical results to synthesize instrument views for direct comparison between data and simulation.

4.1. FLASH simulation

In our FLASH simulation, we draw our experimental assembly in profile view onto a 2.5D, cylindrical grid that is rotationally symmetric to the axis of the plasma plume of the laser drive foil. Our FLASH grid is sized and positioned to allow a complete representation of the evolving plasma from the perspective of the realized instrumentation. The grid extends 800 cells down the symmetric axis, and it extends 320 cells radially. Each cell has $(12.5\ \mu\text{m})^2$, and they sum to $(10\hat{z} \times 4\hat{r})\ \text{mm}^2$. The simulation is initiated on firing a 351 nm, 1 ns square laser pulse carrying 4.5 kJ at a 750 μm-diameter, 4th-order super-Gaussian spot centered on target aligned with the rotational axis of the grid. The laser beams and energy deposition on target are implemented in the laser energy deposition package native to FLASH 4 [23].

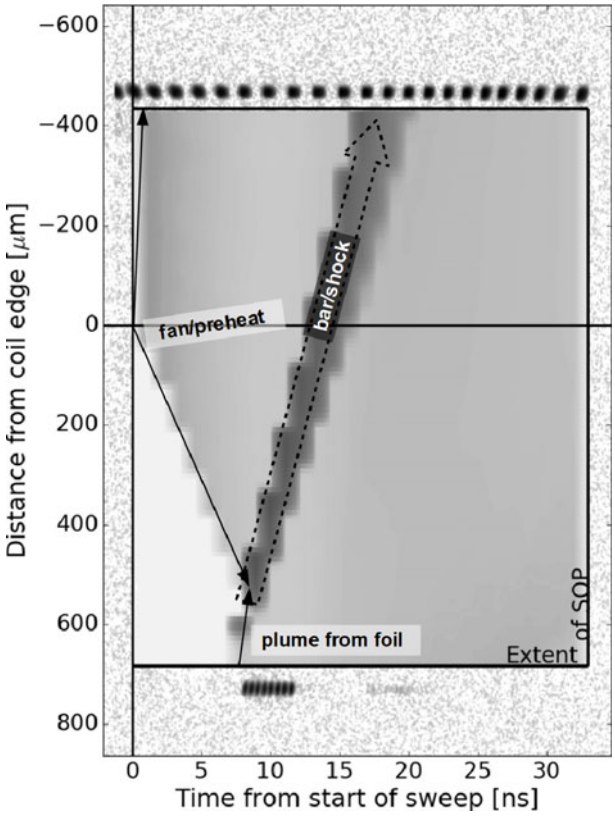

Figure 5. Synthetic ROSS-SOP image replicating Figure 3 built by sweeping the sequence of axial photosphere temperature profiles, i.e., the black curves of Figure 4, through $t_0 + 30$ ns.

Radiative transfer through target materials is implemented with the FLASH native multigroup diffusion (MGD) scheme and with tabulated results of IONMIX simulations[24]. Finally, FLASH implements in its native unsplit staggered mesh (USM) solver numerically stable, fully magnetohydrodynamical calculations by adapting the constrained transport (CT) method[25]. Instead, we elect to use the purely hydrodynamical (UHD) solver because our experimental dataset did not provide any evidence of magnetohydrodynamical effects against which we can test our more complex simulations.

4.2. FLASH results

We show in Figure 4 the time sequence of our FLASH simulations at T_e covering the most important epochs in the evolution of the plasma. In addition, we have computed the depth of formation of the visible continuum, i.e., the 'photosphere' of the plasma seen in the SOP, by integrating the IONMIX-derived absorptivity coefficients from the outside-in. The photosphere is drawn in the T_e plots as a black curve, and it marks where the optical depth $\tau \sim 1$. The axial temperature profile of the photosphere, then, underlies this curve, and a viewer sharing the perspective of the SOP looking in on the plasma from the outside necessarily sees the surface of the gas taking on the temperature of the photosphere as marked[26]. Practically, the photosphere forms where $\rho \sim 10^{-4}$ g/cc, and its radial position is otherwise only weakly dependent on the temperature of the fully ionized HCNO plasma.

Our time sequence in Figure 4 begins on first contact between two flows, one ablated from the MIFEDS wire by preheating, and another driven by the laser from the planar target, at $t_0 + 6$ ns. At this time, we observe the onset of the shock that eventually becomes the bar-like emission feature we identified in Figure 2. By $t_0 + 8$ ns, this shock has become optically thick, i.e., $\tau \gtrsim 1$, or $\rho \gtrsim 10^{-4}$ g/cc with $T_e \sim 1$ MK. On either side of the shock the continuum forms at a cooler $T_e \sim 0.1$ MK. Note that, at this point the 1 MK continuum is displaced both radially and axially from true apex of the shock, and a viewer looking inwards at the true apex sees the ∼0.1 MK continuum. Stepping through the sequence past $t_0 + 8$ ns, the 1 MK continuum inexorably shifts outwards and upwards as it elongates. Onwards from $t_0 + 12$ ns the 1 MK continuum source, i.e., the bar, follows an inertial trajectory across the foreground of the MIFEDS arc as first remarked in Figure 2. Note that, the nose of the bow shock is in fact stagnated by the MIFEDS arc. However, it becomes obscured by cooler gas in the perspective of the SOP at any time except around first contact near $t_0 + 6$ ns, or when the 1 MK continuum overtakes it just before $t_0 + 12$ ns.

Observationally, the difference in the photosphere temperature is immediately consequential. For an observer viewing the plasma in the 1.5–6.5 eV SOP band, the Rayleigh–Jeans flux is proportional to T_e; hence, the cooler, ∼0.1 MK photosphere appears at least proportionately dimmer than the ∼1 MK photosphere. With this flux–temperature relation in mind, we produced in Figure 5 a synthetic streak image to match the perspective of Figure 3. By inspection, we have entirely reproduced the plasma hydrodynamics we previously identified. Crucially, we reproduced the absence of the stagnant apex of the bow shock, and we were able to ascertain its fate.

5. Conclusion

In this article, we reproduced some of the procedures and outcomes of our experiments to recreate the interactions between a fast stellar wind and an evaporating exoplanetary atmosphere using OMEGA facilities. We demonstrated the use of the ROSS-SOP streak camera to continuously record the evolution of spatially resolved optical sources in the experimental plasma. Although the streak images were confusing at first glance, predictive numerical simulations of the experiment using the FLASH code with realistic materials and radiative transfer modeling allowed even unexpected emission features to become understood as a consequence of instrumental perspective and optical depth of the gas.

In a serendipitous twist, in being unable to fully reconstruct the experimental hydrodynamics from the limited perspective of the SOP alone, we demonstrated the necessity of designing laboratory astrophysics experiments to avoid similar limitations of real observations. In our reconciliation of synthetic and experimental images, we also demonstrated how we can overcome the limitations of real experiments using predictive numerical simulations.

Acknowledgements

This work was made possible thanks to the DOE NLUF program DE-FOA-0001568, the Data Analysis and Visualization CyberInfrastructure program OCI-0959097, Rice University, and the Laboratory for Laser Energetics.

References

1. P. Hoeflich, P. Kumar, and J. C. Wheeler, (eds), *Cosmic Explosions in Three Dimensions* (Cambridge University Press, 2004).
2. A. Koenigl, Astrophys. J. Lett. **370**, L39 (1991).
3. J. H. Kastner, D. P. Huenemoerder, N. S. Schulz, C. R. Canizares, and D. A. Weintraub, Astrophys. J. **567**, 434 (2002).
4. B. Stelzer and J. H. M. M. Schmitt, Astron. Astrophys. **418**, 687 (2004).
5. J. Patterson, Proc. Astron. Soc. Pacific **106**, 209 (1994).
6. G. E. Romero, R. A. Sunyaev, and T. Belloni, (eds), *Jets at All Scales* (Cambridge University Press, 2011).
7. B. M. Gaensler and P. O. Slane, Ann. Rev. Astron. Astrophys. **44**, 17 (2006).
8. I. R. Stevens, J. M. Blondin, and A. M. T. Pollock, Astrophys. J. **386**, 265 (1992).
9. C. F. McKee and D. J. Hollenbach, Ann. Rev. Astron. Astrophys. **18**, 219 (1980).
10. D. van Buren, A. Noriega-Crespo, and R. Dgani, Astron. J. **110**, 2914 (1995).
11. P. Hartigan, A. Frank, J. M. Foster, B. H. Wilde, M. Douglas, P. A. Rosen, R. F. Coker, and B. E. Blue, Astrophys. J. **736**, 29 (2011).
12. J. López-Santiago, M. Miceli, M. V. del Valle, G. E. Romero, R. Bonito, J. F. Albacete-Colombo, V. Pereira, E. de Castro, and F. Damiani, Astrophys. J. Lett. **757**, L6 (2012).
13. D. E. Osterbrock, *Astrophysics of Gaseous Nebulae and Active Galactic Nuclei* (University Science Books, 1989).
14. N. Calvet and E. Gullbring, Astrophys. J. **509**, 802 (1998).
15. P. Hartigan and A. Wright, Astrophys. J. **811**, 12 (2015).
16. O. V. Gotchev, J. P. Knauer, P.-Y. Chang, N. W. Jang, M. J. Shoupe III, D. D. Meyerhofer, and R. Betti, Rev. Sci. Instrum. **80**, 043504 (2009).
17. B. Fryxell, K. Olson, P. Ricker, F. X. Timmes, M. Zingale, D. Q. Lamb, P. MacNeice, R. Rosner, J. W. Truran, and H. Tufo, Astrophys. J. Suppl. **131**, 273 (2000).
18. T. R. Boehly, D. L. Brown, R. S. Craxton, R. L. Keck, J. P. Knauer, J. H. Kelly, T. J. Kessler, S. A. Kumpan, S. J. Loucks, S. A. Letzring, F. J. Marshall, R. L. McCrory, S. F. B. Morse, W. Seka, J. M. Soures, and C. P. Verdon, Opt. Commun. **133**, 495 (1997).
19. J. Katz, J. S. Ross, C. Sorce, and D. H. Froula, J. Instr. **8**, C12009 (2013).
20. M. J.-E. Manuel, A. B. Zylstra, H. G. Rinderknecht, D. T. Casey, M. J. Rosenberg, N. Sinenian, C. K. Li, J. A. Frenje, F. H. Séguin, and R. Petrasso, Rev. Sci. Instrum. **83**, 063506 (2012).
21. J. E. Miller, T. R. Boehly, A. Melchior, D. D. Meyerhofer, P. M. Celliers, J. H. Eggert, D. G. Hicks, C. M. Sorce, J. A. Oertel, and P. M. Emmel, Rev. Sci. Instrum. **78**, 034903 (2007).
22. P. A. Jaanimagi, R. Boni, D. Butler, S. Ghosh, W. R. Donaldson, and R. L. Keck, Proc. SPIE **5580**, 408 (2005).
23. FLASH Center 2015, Flash Users Guide, Tech. Rep., University of Chicago FLASH Center for Computational Science.
24. J. J. Macfarlane, Comput. Phys. Commun. **56**, 259 (1989).
25. C. R. Evans and J. F. Hawley, Astrophys. J. **332**, 659 (1988).
26. D. F. Gray, *Observation and Analysis of Stellar Photospheres* (Cambridge University Press, 2008).